Grain Refinement Mechanism and Evolution of Dislocation Structure of Co Cr Mo Alloy Subjected to High-Pressure Torsion

doi: 10.2320/matertrans.M2016052

Materials Transactions, Vol. 57, No. 7 (2016) pp. 1109 to 1118

Grain Refinement Mechanism and Evolution of Dislocation Structure of Co–Cr–Mo Alloy Subjected to High-Pressure Torsion

Murat Isik[1], Mitsuo Niinomi[2,*], Huihong Liu[2], Ken Cho[3], Masaaki Nakai[2], Zenji Horita[4,5], Shigeo Sato[6], Takayuki Narushima[7], Hakan Yilmazer[8] and Makoto Nagasako[2]

[1]*Graduate Student, Department of Materials Science, Tohoku University, Sendai 980–8579, Japan*
[2]*Institute for Materials Research, Tohoku University, Sendai 980–8577, Japan*
[3]*Graduate School of Engineering, Osaka University, Osaka 565–0871, Japan*
[4]*Department of Materials Science and Engineering, Faculty of Engineering, Kyushu University, Fukuoka 819–0395, Japan*
[5]*WPI, International Institute for Carbon-Neutral Energy Research (WPI-I2CNER), Kyushu University, Fukuoka 819–0395, Japan*
[6]*Graduate School of Science and Engineering, Ibaraki University, Hitachi 316–8511, Japan*
[7]*Department of Materials Processing, Tohoku University, Sendai 980–8579, Japan*
[8]*Department of Metallurgical and Materials Science Engineering, Yildiz Technical University, Istanbul 34220, Turkey*

Ultrafine-grained materials often possess superior mechanical properties owing to their small grain size. The high-pressure torsion (HPT) process is a severe plastic deformation method used to induce ultra-large strain and produce ultrafine grains. In this study, the grain refinement mechanisms in the Co–28Cr–6Mo (CCM) alloy, evolution of dislocation density as a result of HPT and its effects on mechanical properties were investigated. The dislocation density and subgrain diameter were also calculated by X-ray line profile analysis. The microstructure of the CCM alloy subjected to HPT processing (CCM_{HPT}) was evaluated as a function of torsional rotation number, N and equivalent strain, ε_{eq}. Strain-induced $\gamma \rightarrow \varepsilon$ transformation in neighboring ultrafine grains is observed in CCM_{HPT} processed at $\varepsilon_{eq} = 2.25$ and $\varepsilon_{eq} = 4.5$. Low-angle crystal rotation around the [110] fcc direction occurs in different locations in the same elongated grain neighboring ultrafine grains, which suggests the formation of low-angle grain boundaries in CCM_{HPT} processed at $\varepsilon_{eq} = 2.25$ and $\varepsilon_{eq} = 4.5$. Two possible grain refinement mechanisms are proposed. The maximum dislocation densities, which are 2.8×10^{16} m^{-2} in γ phase and 3.8×10^{16} m^{-2} in ε phase, and maximum subgrain diameters, which are 21.2 nm in γ phase and 36 nm in ε phase, are achieved in CCM_{HPT} processed at $\varepsilon_{eq} = 9$. HPT processing causes a substantial increase in the tensile strength and hardness owing to the grain refinement and a significant increase in the volume fraction of ε phase and dislocation density. [doi:10.2320/matertrans.M2016052]

(Received February 15, 2016; Accepted April 4, 2016; Published May 20, 2016)

Keywords: *cobalt-chrome-molybdenum alloys, high-pressure torsion, strain-induced ε martensite phase, grain refinement mechanism, dislocation density*

1. Introduction

To date, several techniques of severe plastic deformation (SPD), such as equal-channel angular pressing (ECAP), high-pressure torsion (HPT), accumulative roll bonding (ARB), and cyclic extrusion compression (CEC) are being used to process coarse-grained materials to realize ultrafine microstructure by inducing heavy strain.[1–4] Among these techniques, HPT processing induces the highest strain, which achieves the smallest grain size, and is most preferable for laboratory applications.[1,3,5–8]

Previously, various metallic materials have been subjected to HPT processing such as titanium, aluminum, steel and magnesium.[5,9–13] Recent studies have also reported that the microstructure of pure cobalt (Co) can be refined to the nanoscale by HPT, thereby resulting in promising mechanical properties such as tensile strength and hardness. The ultimate tensile strength and hardness of nanocrystalline pure Co are 750 MPa and 3530 MPa, while those of the coarse-grained pure Co are 210 MPa and 1700 MPa, respectively.[14,15] In addition, HPT has been applicable for achieving grain refinement in Co-Cr-Mo alloys, which have attracted wide interest owing to their spectacular mechanical properties such as high tensile strength and hardness.[16–18] Furthermore, inducing strain to Co-Cr-Mo alloys leads to strain-induced $\gamma \rightarrow \varepsilon$ phase transformation.[19] Therefore, HPT processing that results in enormous strain in metallic materials may induce the $\gamma \rightarrow \varepsilon$ phase transformation in Co-Cr-Mo alloys. The formation of the ε phase is another effect of HPT processing for improving the strength of Co-Cr-Mo alloys, in addition to the formation of ultrafine-grained microstructure, and they strongly affect the deformation behavior in Co-Cr-Mo alloys subjected to SPD.[2,19–24] Increasing tensile strength and hardness in the Co-Cr-Mo alloy using HPT processing has been reported in a previous study.[25]

The present investigation was motivated by two main subjects. First, the production of ultrafine-grained materials via HPT processing has gained significant importance from both academic and industrial aspects. Therefore, there is a need to investigate the grain refinement mechanism during HPT processing to enable further developments for producing ultrafine-grained materials. So far, various investigations have been reported about the evolution of microstructure and change in mechanical properties of ultrafine-grained materials fabricated by different SPD techniques.[2,3,26,27] However, the grain refinement mechanism of Co-Cr-Mo alloys in particular has not been clearly identified, and there are only a limited number of findings about the deformation mechanism of pure Co during SPD.[24] Therefore, the grain refinement mechanism needs to be clarified for further developments in producing ultrafine-grained Co-Cr-Mo alloys and for improving their mechanical properties.

An additional objective of this study is to explain the evolution of the dislocation structure produced during HPT pro-

*Corresponding author, E-mail: niinomi@imr.tohoku.ac.jp

cessing. The large amounts of dislocations induced by HPT processing are crucial elements in the grain refinement process. Controlling the dynamic balance between the generation and annihilation of dislocations plays an important role in grain refinement.[28] Further, the $\gamma \rightarrow \varepsilon$ phase transformation may contribute to grain refinement via the formation of ε platelets, which may further be refined, and these ε platelets may cause the refinement of γ phase grains by subdividing them. Consequently, it is concluded that controlling the phase transformation and dislocation structure is related to grain refinement. A better understanding of the grain refinement mechanism may help to generate ultrafine-grained materials.

Therefore, the aim of this work is to elucidate the grain refinement mechanism and evolution of dislocation structures in Co–28Cr–6Mo alloy during HPT processing, and to clarify their effect on the mechanical properties of this HPT-processed alloy.

2. Experimental Procedures

2.1 Materials

A cylindrical rod of a hot forged Co–28Cr–6Mo (mass%, CCM) alloy with a diameter of 25 mm and a length of 50 mm was used in this study. The chemical composition of the CCM alloy is listed in Table 1. The rod was subjected to a solution treatment at 1473 K for 3.6 ks in vacuum (hereafter designated as CCM_{ST}). The CCM_{ST} rod was machined to disk-shaped specimens with a diameter of 10 mm and a thickness of 1 mm for HPT processing. In addition, some of the CCM_{ST} plates were subjected to cold rolling with a thickness reduction ratio of 50% (CCM_{CR}).

2.2 High-pressure torsion (HPT)

The CCM_{ST} disk was subjected to HPT processing (hereafter designated as CCM_{HPT}) under quasi-constrained conditions, through which the lower anvil was rotated for 0.25, 0.5, 1, 2 and 5 times (N) with a rotation speed of 1 rpm (0.1220 rad s^{-1}) under a pressure of 6 GPa in air at room temperature. The equivalent strain, ε_{eq}, at a distance r from the disk center was estimated by the following equation:[1]

$$\varepsilon_{eq} = 2\pi r N / t\sqrt{3} \quad (1)$$

where N is the rotation number and t is the specimen thickness. ε_{eq} was calculated according to eq. (1) as a function of distance from the disk center for $N = 0.25$, 0.5, 1, 2 and 5. As a result, the values of ε_{eq} are 2.25, 4.5, 9, 18 and 45 for $N =$ 0.25, 0.5, 1, 2 and 5 at the half radius ($r = 2.5$ mm), respectively.

2.3 Microstructural characterization

The microstructures of CCM_{ST} and CCM_{HPT} processed at $\varepsilon_{eq} = 2.25$, 9, 18, and 45 at the half radius r_h ($r = r_h = 2.5$ mm) were characterized by X-ray diffractometry (XRD) using monochromated Cu Kα_1 radiation with an operation voltage of 40 kV and a tube current of 40 mA and a transmission electron microscopy (TEM) at an acceleration voltage of 200 kV. The TEM analyses were also carried out at r_h position that is schematically shown in Fig. 1 (a).

For TEM sample preparation, the CCM_{HPT} disk was fixed between two silicon substrates using an epoxy and then cut parallel to the cross section near the center of the CCM_{HPT} disk to prepare a thin plate. The plate was wet polished using water-proof emery papers up to #2400. Then, a copper ring with a diameter of 3 mm was fixed on the polished plate at the r_h position using the epoxy. The thickness was further reduced to less than 20 μm using a dimple grinder and an ion milling. Additional information about the TEM sample preparation was detailed and illustrated in a previous study.[10]

2.4 X-ray line profile analysis

The microstructures and dislocation structures of CCM_{ST}, CCM_{CR} and CCM_{HPT} were investigated by X-ray line profile analysis (XLPA)[29] using a convolution multiple profile (CMWP) fitting method.[30] The measurement position for XLPA analysis is shown in Fig. 1 (b). The obtained XRD profiles were fitted using a theoretical profile, I, which is a product of the convolution of size, strain, and instrumental profiles:

$$I = I_S \otimes I_m \otimes I_i \quad (2)$$

where I_s is the profile of the size of the smallest unit of a crystal aggregate, I_m is the profile of the microstrain, and I_i is the

Table 1 Chemical composition of hot forged CCM alloy. (mass%)

Alloying element	Co	Cr	Mo	Ni	Mn	Si	C	N	Fe
	Bal.	27.7	5.87	<0.01	0.58	0.50	0.045	0.14	<0.1

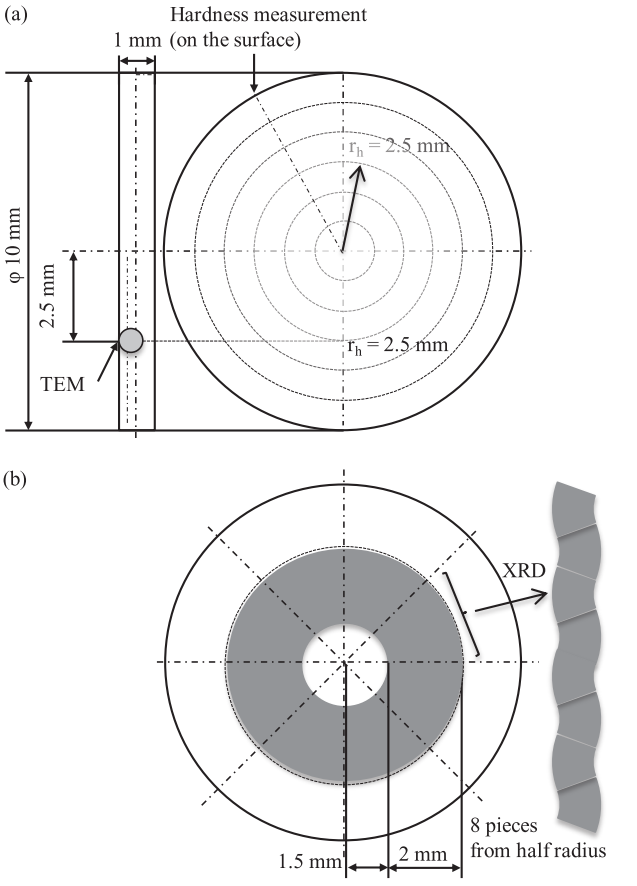

Fig. 1 (a) Positions for TEM analysis and hardness measurement, and (b) XRD analysis on disk sample.

profile of the instrument effect.

It has been reported that, crystallite diameter obtained from XLPA indicates the subgrain or cell diameter bounded by small-angle grain boundaries or dipolar walls.[9] The area-weighted size $\langle X\rangle_{\text{area}}$ was then estimated[30] by CMWP fitting as follows;

$$I_{\text{S}}(s) = \int_0^{\infty} M\frac{\sin^2(M\pi s)}{(\pi s)^2}\text{erfc}\left[\frac{\log\left(\frac{M}{m}\right)}{\sqrt{2}\sigma}\right]\text{d}M \quad (3)$$

$$\langle X\rangle_{\text{area}} = m\exp(2.5\sigma^2) \quad (4)$$

where m and σ are the parameters of the lognormal distribution function, $\log m$ is the median and σ is the variance of the normal function. The variable of the size profile s can be expressed as;

$$s = \frac{2\sin\theta}{\lambda} - \frac{2\sin\theta_{\text{B}}}{\lambda} \quad (5)$$

where λ is the wavelength of the X-rays. The values of 2θ and $2\theta_{\text{B}}$ are the scattering angle and the exact Bragg position, respectively.

I_{m} used in CMWP fitting was presented with its Fourier transform equation[31] as follows:

$$I_{\text{m}}(s) = \int \exp\{-2\pi^2L^2k^2\langle\varepsilon_{k,L}{}^2\rangle\}\text{d}L \quad (6)$$

where k and L are the absolute value of the diffraction vector and the Fourier valuable, respectively. $\langle\varepsilon_{k,L}{}^2\rangle$ is the mean square strain defined as follows:

$$\langle\varepsilon_{k,L}{}^2\rangle = \left(\frac{b}{2\pi}\right)^2\pi\rho C f\left(\frac{L}{R_{\text{e}}}\right) \quad (7)$$

where ρ, C, b, R_{e} and f are the dislocation density, the contrast factor of the dislocations, the absolute value of Burgers vector, the Wilkens function and the effective outer cut-off radius of dislocations, respectively.[31–33] In order to clearly demonstrate the dislocation arrangement during deformation, a suitable dimensionless parameter $M(M = R_{\text{e}}\sqrt{\rho})$ was introduced.[9]

Finally, the instrumental profile (I_{i}) was prepared using the XRD profile of standard LaB_6 powders.

2.5 Mechanical tests

An Instron-type testing machine was used for evaluating the tensile properties of CCM alloys. The tensile tests were conducted at room temperature with a cross-head speed of 8.33×10^{-6} m·s^{-1}, which is equivalent to an initial strain rate of 6.94×10^{-3} s^{-1}. The tensile test specimens were obtained from disk-shaped samples. The geometric shape of the tensile specimens was as described in a previous study.[25] These specimens were wet-polished using water-proof emery papers up to #1500 and thinned to a cross-sectional thickness of 0.5–0.6 mm (i.e., material up to a depth of ~0.2–0.25 mm is removed from the two different surface directions).

Hardness measurements were carried out using a Vickers microhardness tester with a load of 4.9 N for a dwell time of 15 sec on the surface of a coin-shaped specimen as shown in Fig. 1 (a). The surfaces of the specimens were polished to the half radius positions, r_{h} (material up to a depth of ~0.25 mm from the surface direction is removed). The measurements on the surface were performed at an interval of 1 mm from center of the disk-shaped specimen to the edge along the radius direction.

3. Results

3.1 Microstructure

The volume fractions of the ε phases in the CCM_{ST} and CCM_{HPT} specimens were calculated by performing XRD analyses at the r_h positions. Intensities of $\{200\}_\gamma$ and $\{10\bar{1}1\}_\varepsilon$ XRD peaks were integrated and quantitative analyses on the volume fraction of the γ and ε phases were carried out.[34] The corresponding results are shown in Fig. 2. CCM_{ST} only contains single face-centered-cubic (fcc) γ phase. However, there is an obvious evidence for $\gamma\rightarrow\varepsilon$ martensitic transformation during HPT processing. The volume fraction of the ε phase increases to around 87% even with processing at low ε_{eq} (in CCM_{HPT} processed at $\varepsilon_{\text{eq}} = 2.25$). Then, the volume fraction of the ε phase slightly decreases when ε_{eq} exceeds 9, and it subsequently saturates.

With increasing strain during HPT processing, $\gamma\rightarrow\varepsilon$ martensitic transformation occurs as shown in TEM bright field images (see Figs. 3 (a) and (g)) and confirmed by selected area electron diffraction (SAED) pattern (see Fig. 3 (c)) and dark field (DF) images (see Figs. 3 (k) and (l)). According to SAED pattern in Fig. 3 (c), the ε phase has the Shoji-Nishiyama (S-N) orientation relationship[35] with the parent γ phase as $(001)_\varepsilon//(1\bar{1}1)_\gamma$ and $BD//[110]_\varepsilon//[110]_\gamma$. Ultrafine microstructure in the neighborhood of ε martensites has been observed via high-magnification TEM images, as shown in Figs. 3 (b) and (h) and confirmed by SAED patterns in Figs. 3 (e) and (i). Diffracted ring patterns in Figs. 3 (e) and (i) indicate the formation of ultrafine-grained microstructure consisting of dual phases, i.e., a combination of γ and ε phases. Therefore, TEM images in Figs. 3 (a) and (g) present the coarse-grained and ultrafine-grained microstructure of CCM_{HPT} processed at $\varepsilon_{\text{eq}} = 2.25$ and $\varepsilon_{\text{eq}} = 4.5$. Nanocrystalline grains in Figs. 3 (b) and (h) exhibit blurry and wavy morphologies and their grain boundaries show low misorientation angle. In addition, the evolution of $\gamma\rightarrow\varepsilon$ phase transformation

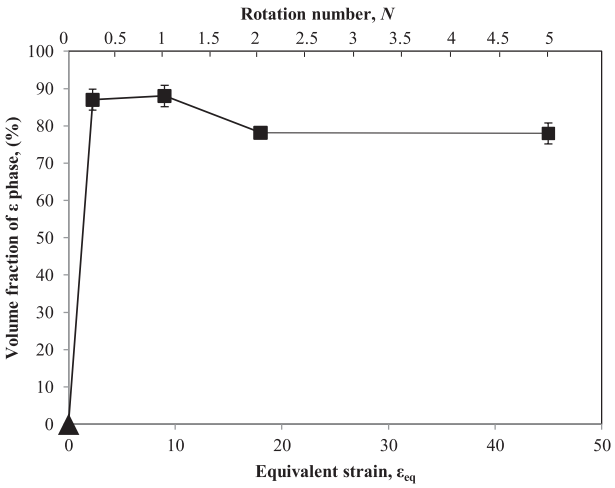

Fig. 2 Volume fractions of ε phases in CCM_{ST} ($\varepsilon_{\text{eq}} = 0$) and CCM_{HPT} processed at $N = 0.25$ ($\varepsilon_{\text{eq}} = 2.25$), $N = 1$ ($\varepsilon_{\text{eq}} = 9$), $N = 2$ ($\varepsilon_{\text{eq}} = 18$), and $N = 5$ ($\varepsilon_{\text{eq}} = 45$) obtained from XRD analyses.

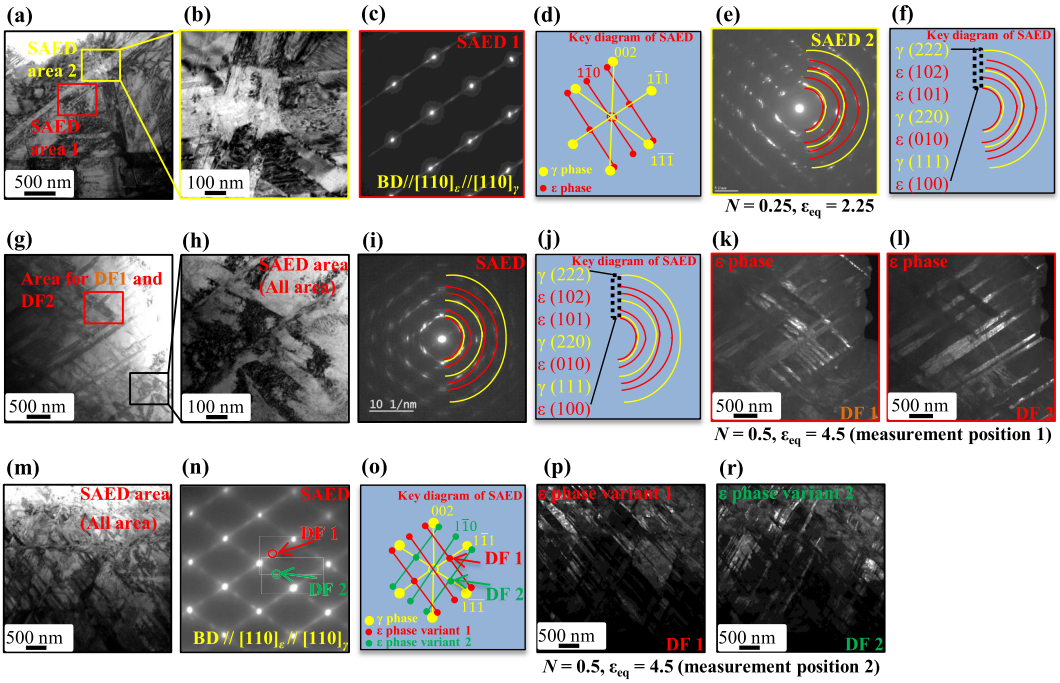

Fig. 3 (a) and (b) TEM bright field images, (c) and (e) SAED patterns corresponding SAED area 1 and 2 in (a), (d) and (f) key diagrams of (c) and (e), respectively, for CCM_{HPT} processed at $\varepsilon_{eq} = 2.25$. (g) and (h) TEM bright field images, (i) SAED pattern corresponding SAED area in (h), (j) key diagram of (i), (k) and (l) DF images corresponding area for DF1 and DF2 in (g), for CCM_{HPT} processed at $\varepsilon_{eq} = 4.5$ (measurement position 1). (m) TEM bright field image, (n) SAED pattern corresponding SAED area in (m), (o) key diagram of (n), and (p) and (r) DF images taken from ε phase variant 1 and 2 spots shown with arrows in (n) for CCM_{HPT} processed at $\varepsilon_{eq} = 4.5$ (measurement position 2). γ phase, ε phase variant 1, and ε phase variant 2 are indicated in yellow, red and green, respectively, in the key diagrams of the SAED patterns.

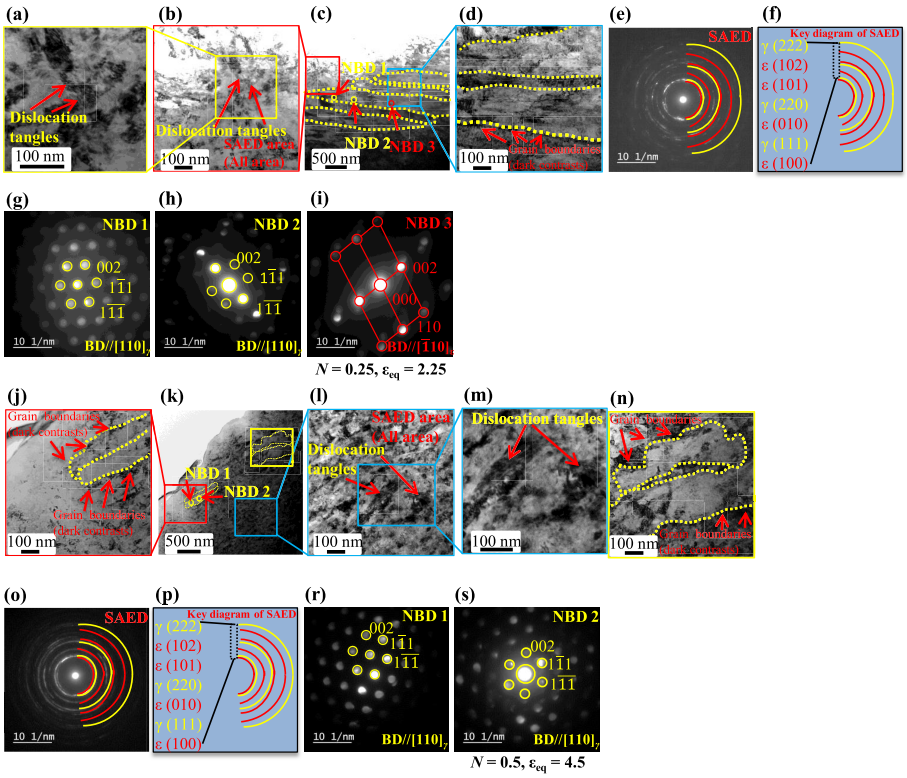

Fig. 4 (a), (b), (c) and (d) TEM bright field images, (e) SAED pattern corresponding SAED area in (b), (f) key diagram of (e), and (g), (h) and (i) nanobeam diffraction patterns of areas shown with arrows as NBD 1, 2 and 3 in (c), for CCM_{HPT} processed for $\varepsilon_{eq} = 2.25$. (j), (k), (l), (m) and (n) TEM bright field images, and (o) SAED pattern corresponding SAED area in (l), (p) key diagram of (o), (r) and (s) nanobeam diffraction patterns of areas shown with arrows as NBD 1 and 2 in (k), for CCM_{HPT} processed for $\varepsilon_{eq} = 4.5$.

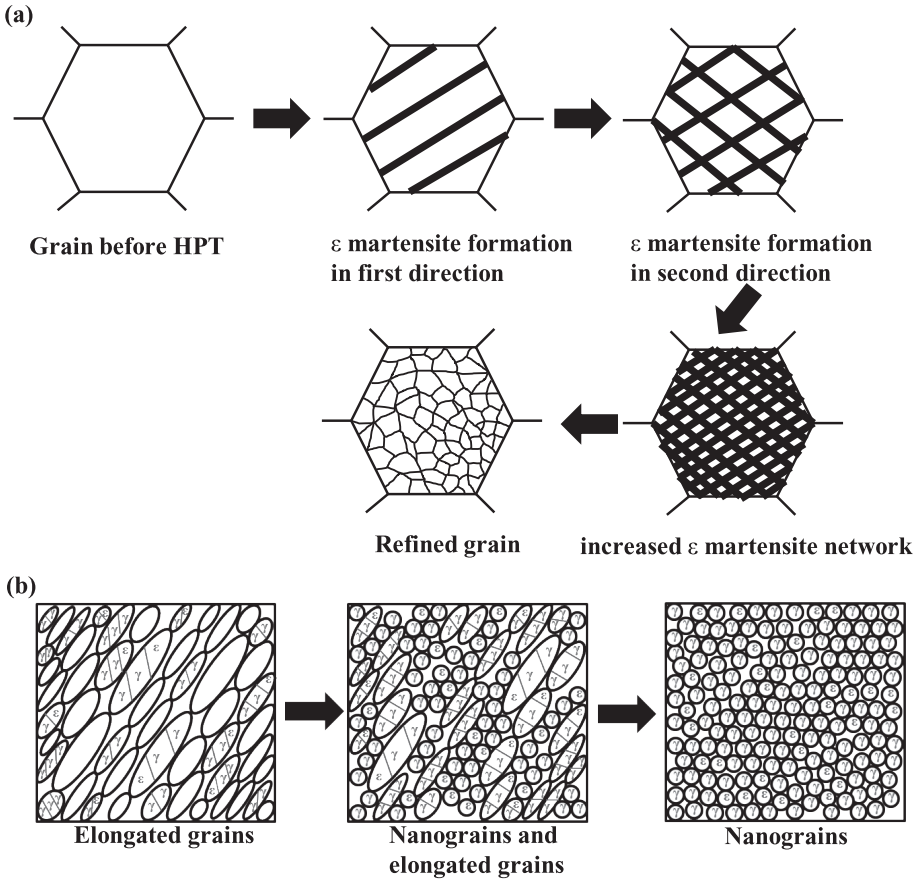

Fig. 5 Schematic illustration of grain refinement process through (a) mechanism related to $\gamma \rightarrow \varepsilon$ martensitic transformation and (b) mechanism related to elongated grains.

can be identified in CCM_{HPT} processed at $\varepsilon_{eq} = 4.5$. The average width of the ε martensite platelets is around 100 nm in CCM_{HPT} processed at $\varepsilon_{eq} = 4.5$. Figure 3 (m) shows the intersecting network of ε martensite platelets. The occurrence of $\gamma \rightarrow \varepsilon$ martensitic transformation and existence of two different ε phase variants are confirmed by the SAED pattern in Fig. 3 (n). The relationship of $(001)_\varepsilon // (1\bar{1}1)_\gamma$ and $BD // [1\bar{1}0]_\varepsilon // [110]_\gamma$ for ε phase variant 1 and that of $(001)_\varepsilon // (\bar{1}\bar{1}1)_\gamma$ and $BD // [110]_\varepsilon // [110]_\gamma$ for ε phase variant 2 can also be identified. The intersecting ε martensite platelets in the network are aligned in different directions. The average width of ε martensite platelets is around 80 nm according to Figs. 3 (p) and (r).

In Figs. 4 (c) and (k), a large number of ultrafine grains were seen coexisting with some micro-scale grains. HPT processing causes a microstructure consists of coarse grained and nanocrystallines at CCM_{HPT} processed at $\varepsilon_{eq} = 2.25$ and $\varepsilon_{eq} = 4.5$. In addition, TEM images in Fig. 4 suggest that the elongated grains are possibly subdivided into the equiaxed ultrafine grains. Nanobeam diffraction (NBD) patterns with a small misorientation angle are detected in neighboring positions in the same elongated grain, indicating the occurrence of low-angle crystal rotation around [110] γ direction inside the elongated grains for both CCM_{HPT} processed at $\varepsilon_{eq} = 2.25$ (see Figs. 4 (c), (g) and (h)) and CCM_{HPT} processed at $\varepsilon_{eq} = 4.5$ (see Figs. 4 (j), (r) and (s)). In addition, the ε phase transformation occurs, as suggested in Fig. 4 (i) for CCM_{HPT} processed at $\varepsilon_{eq} = 2.25$. The crystal rotation and formation of the ε phase occur in the same elongated grain. Newly formed nanograins are presented in TEM bright field images in Figs. 4 (b) and (l) and confirmed by diffracted rings in Figs. 4 (e) and (o). Nanocrystalline grains in Figs. 4 (b) and (l) exhibit blurry and wavy morphologies. At higher magnifications, it is possible to distinguish the low-angle grain boundaries and existence of dislocation tangles,[36] which indicates high strain and high density of dislocations in Figs. 4 (b), (a), (l) and (m). In addition, TEM SAED patterns in Figs. 4 (e) and (o) indicate that diffracted beams tend to form ring patterns at CCM_{HPT} processed at $\varepsilon_{eq} = 4.5$ compared to CCM_{HPT} processed at $\varepsilon_{eq} = 2.25$, indicating that grain refinement develops with increasing ε_{eq}. Most of the elongated grains that are ~300 nm in width and ~2.5 μm in length show a high dislocation density for CCM_{HPT} processed at $\varepsilon_{eq} = 2.25$. Further increasing ε_{eq} with increasing N changes the morphology of the elongated grains. The width and length of the elongated grains decrease with increasing ε_{eq}. Most of the elongated grains in CCM_{HPT} processed at $\varepsilon_{eq} = 4.5$ are ~100 nm in width and ~900 nm in length, as shown in Figs. 4 (j) and (k). In addition, there is a decreasing in prevalence of elongated grains in CCM_{HPT} processed at $\varepsilon_{eq} = 4.5$ compared to that in CCM_{HPT} processed at $\varepsilon_{eq} = 2.25$. In addition, high magnification TEM bright field images in Figs. 4 (d) and (n) show that elongated grains contain subgrains or cells. Figure 5 summarizes the the occurrence of grain refinement induced by $\gamma \rightarrow \varepsilon$ transformation and subdivision of elongated grains according to Figs. 3 and 4.

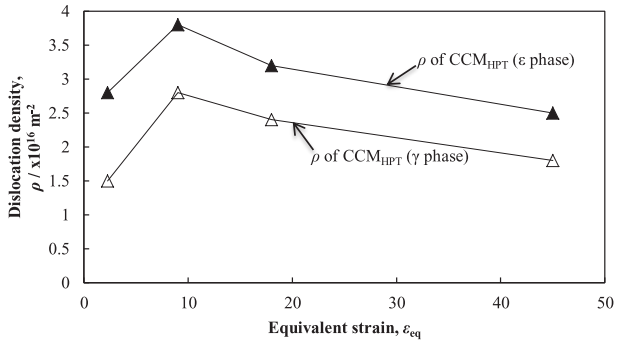

Fig. 6 Dislocation densities (ρ) in γ and ε phase of CCM_{HPT} alloys as a function of ε_{eq}.

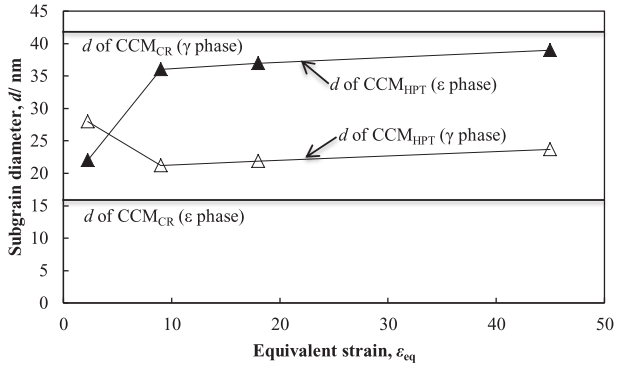

Fig. 7 Subgrain diameters (d) of γ and ε phase of CCM_{HPT} alloys as a function of ε_{eq} in comparison with those of CCM_{CR} (horizontal lines).

Dislocation densities (ρ) of CCM_{HPT} alloys as a function of ε_{eq} are shown in Fig. 6. The dislocation densities for γ and ε phases in CCM_{CR} are smaller than 10^{13} m^{-2} and ~0.6 × 10^{16} m^{-2}, respectively. Firstly, HPT processing causes the accumulation of dislocations and dislocation densities in γ and ε phases significantly increase through HPT processing to $\varepsilon_{eq} = 2.25$ compared to that in CCM_{CR}. The dislocation densities continue to increase, and then, they reach the maximum ~2.8 × 10^{16} m^{-2} for γ phase and ~3.8 × 10^{16} m^{-2} for ε phase at $\varepsilon_{eq} = 9$. A balance between accumulation and annihilation of dislocations is achieved at $\varepsilon_{eq} = 9$. The latter, dislocation densities tend to decrease with increasing ε_{eq} through HPT processing.

Subgrain diameters (d) of CCM_{HPT} alloys as a function of ε_{eq} in comparison with those of CCM_{CR} (horizontal lines) are shown in Fig. 7. The subgrain diameter of the γ phase in CCM_{CR} is larger than that in CCM_{HPT}, while that of the ε phase in CCM_{CR} is smaller than that in CCM_{HPT}. The subgrain diameter of the γ phase decreases, while that of the ε phase increases with HPT processing. After ε_{eq} is over than 9, subgrain diameters of γ and ε phases in CCM_{HPT} are found to be saturated. Figure 8 shows the dislocation arrangement parameters, M, of CCM_{HPT} alloys as a function of ε_{eq}. M parameter gives valuable information about the arrangement of dislocations.[9] The $M > 1$ indicates weak screening of dislocation fields, while $M < 1$ indicates strong screening of dislocation fields. When M is smaller than 1, the dislocations are suitably arranged in CCM_{HPT}. The M parameters of the γ and ε phases are ~0.96 and ~1.17 at $\varepsilon_{eq} = 2.25$, respectively, and then, they

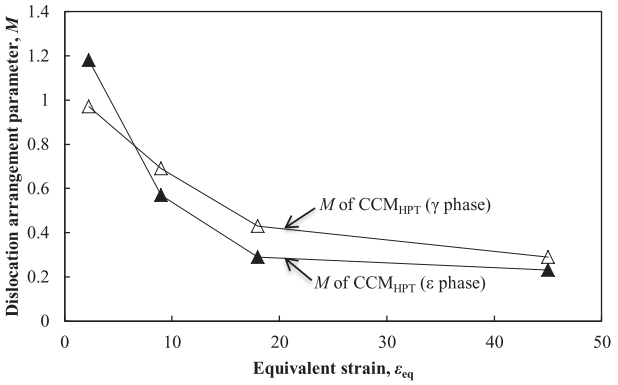

Fig. 8 Dislocation arrangement parameters (M) of γ and ε phase of CCM_{HPT} alloys as a function of ε_{eq}.

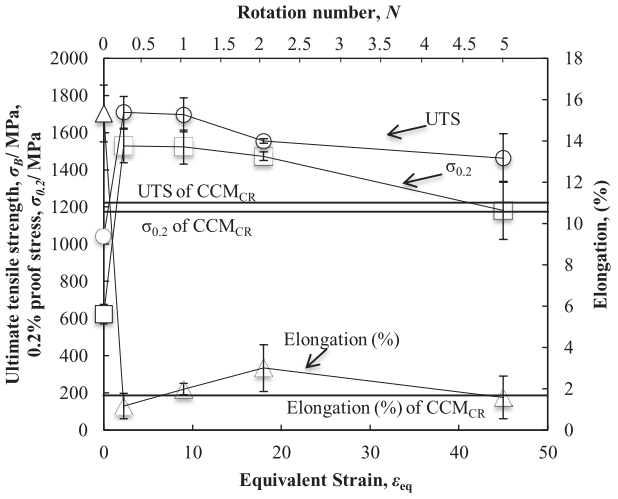

Fig. 9 Tensile properties of CCM_{ST} ($\varepsilon_{eq} = 0$), CCM_{CR} (horizontal lines), and CCM_{HPT} processed at $N = 0.25$ ($\varepsilon_{eq} = 2.25$), $N = 1$ ($\varepsilon_{eq} = 9$), $N = 2$ ($\varepsilon_{eq} = 18$) and $N = 5$ ($\varepsilon_{eq} = 45$) as a function of equivalent strain (ε_{eq}) or rotation number (N).

decrease with increasing ε_{eq} through HPT processing. The increasing ε_{eq} from $\varepsilon_{eq} = 2.25$ to $\varepsilon_{eq} = 9$ causes a decrease in M parameter due to the arrangement of dislocations, even though the dislocation density in CCM_{HPT} at $\varepsilon_{eq} = 9$ is higher than that in CCM_{HPT} processed at $\varepsilon_{eq} = 2.25$. Furthermore, the M parameter of CCM_{HPT} decreases from $\varepsilon_{eq} = 9$ to $\varepsilon_{eq} = 45$, owing to the arrangement of dislocations and decreased dislocation density.[37]

3.2 Mechanical properties

Figure 9 shows the tensile properties of CCM_{ST} ($\varepsilon_{eq} = 0$), CCM_{CR} (horizontal lines) and CCM_{HPT} processed at ε_{eq} = 2.25, 9, 18 and 45, respectively. It is shown in Fig. 9 that ultimate tensile strength (UTS) of CCM_{HPT} is greater than those of CCM_{ST} and CCM_{CR}. The $\gamma \rightarrow \varepsilon$ martensitic transformation, grain refinement, and increase in dislocation density through HPT processing lead to a substantial increase in the mechanical strength. The UTS, 0.2% proof stress, and elongation of CCM_{ST} are ~1041 MPa, ~623 MPa, and ~15%, respectively. CCM_{HPT} processed at $\varepsilon_{eq} = 2.25$ has the greatest UTS and 0.2% proof stress, i.e., ~1709 MPa and ~1528 MPa, respectively. For CCM_{HPT} processed at $\varepsilon_{eq} = 9$, the UTS is around 1696 MPa while the 0.2% proof stress is around 1522 MPa.[10]

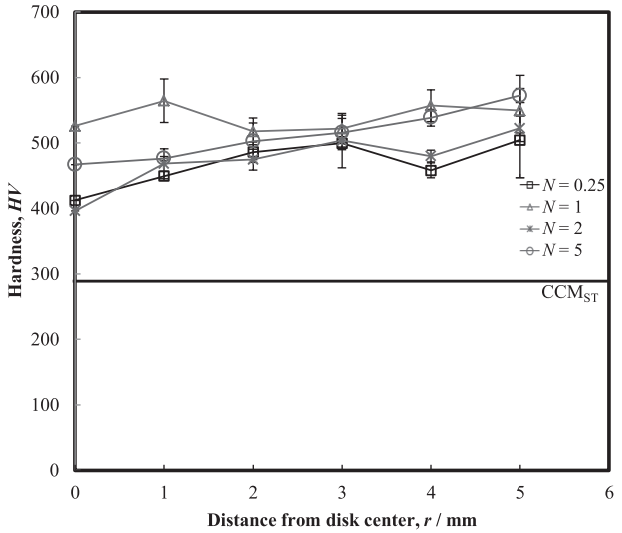

Fig. 10 Hardness distributions of CCM_{ST} (horizontal line), and CCM_{HPT} processed at $N = 0.25$ ($\varepsilon_{eq} = 2.25$), $N = 1$ ($\varepsilon_{eq} = 9$), $N = 2$ ($\varepsilon_{eq} = 18$) and $N = 5$ ($\varepsilon_{eq} = 45$) as a function of distance from disk center.

Further, the UTS of CCM_{HPT} decreases slightly with increasing ε_{eq} to 18, and then saturates as the ε_{eq} further increases.[10] The elongation of CCM_{HPT} processed at different ε_{eq} shows close values, which are much lower than that of CCM_{ST} and comparable with that of CCM_{CR}.

Hardness distributions of CCM_{ST} (horizontal line) and CCM_{HPT} processed at $\varepsilon_{eq} = 2.25$ ($N = 0.25$), $\varepsilon_{eq} = 9$ ($N = 1$), $\varepsilon_{eq} = 18$ ($N = 2$) and $\varepsilon_{eq} = 45$ ($N = 5$) are shown in Fig. 10. Hardness of CCM alloy increases significantly through HPT processing compared to that in the ST condition. It is also realized that the hardness of CCM_{HPT} increases from the disk center to the edge. The hardness of CCM_{HPT} seems to be almost constant for different N at the half radius position in the surface of specimens. CCM_{HPT} processed at $\varepsilon_{eq} = 9$ ($N = 1$) and $\varepsilon_{eq} = 45$ ($N = 5$) have the greatest hardness at the center and edge positions, respectively.

4. Discussion

4.1 Microstructural evolution

Figure 2 showed that the volume fraction of the ε phase in CCM alloys significantly increased through HPT processing at $\varepsilon_{eq} = 2.25$ and 9 in comparison to that in the ST condition. The volume fraction of the ε phase then slightly decreased with increasing ε_{eq} to 18, and saturates with further increasing ε_{eq}. Generally, the phase transformations were enhanced by increasing ε_{eq}.[2,38] However, previous studies on pure Co[15,39] and steel[5] processed by HPT have reported the decrease in the volume fraction of ε phase through HPT processing, which could be attributed to a possible reverse transformation.[25] It has been reported that a reverse $\varepsilon \rightarrow \gamma$ transformation occurred in Co, when the grain diameter was below 100 nm. Local fcc packing sequences were formed by deformation in nanocrystalline pure Co. Increasing deformation led to accumulation of a large number of fcc packing sequences, and $\varepsilon \rightarrow \gamma$ transformation occurred.[15,25,39,40] These views can be used to interpret the decrease in the volume fraction of ε phase in CCM_{HPT} alloy after increasing ε_{eq} to 18 in the present study.

Figure 3 showed the $\gamma \rightarrow \varepsilon$ martensitic transformation accompanied with the occurrence of grain refinement in CCM_{HPT} alloys. In previous studies, it has been reported that the $\gamma \rightarrow \varepsilon$ martensitic transformation may contribute to grain refinement in two respects for pure Co.[24] First aspect, the $\gamma \rightarrow \varepsilon$ martensitic transformation causes the formation of refined ε platelets. The formation of ε martensites in different directions results in an intersecting network structure of ε martensites. This network structure can lead to refinement of coarse martensite platelets into nanoscale. Second aspect, already formed ε platelets are considered to be grain boundaries to subdivide the γ grains thereby inducing the γ grain refinement[24]. A similar effect to the abovementioned second aspect has been reported on mechanical twins in stainless steel,[41] in which twin-twin intersections subdivided coarse grains into sub-microscale blocks, and these gradually resulted in the formation of subgrain boundaries. These blocks eventually transformed into equiaxed refined grains via the development of subgrain boundaries. In the present study, an intersecting network composed of densely distributed ε martensite plates with various variants and nanograined microstructure can be observed simultaneously in CCM_{HPT} alloy when ε_{eq} increases to 4.5. These results support the grain refinement mechanism related to $\gamma \rightarrow \varepsilon$ martensitic transformation as mentioned above.

TEM images in Fig. 4 give information about another grain refinement mechanism. The microstructure of CCM_{HPT} processed at $\varepsilon_{eq} = 2.25$ mainly consists of parallel bands of elongated grains. These extended parallel band boundaries are also called lamellar-type boundaries.[23] The boundaries of elongated grains with dark contrasts were shown with red arrows in Figs. 4 (d), (j) and (n). Nanobeam diffraction patterns indicate the occurrence of low-angle crystal rotation around the [110] γ direction and formation of ε phase in one elongated γ grain in CCM_{HPT} alloys. The occurrence of crystal rotation is attributed to dislocations that are distributed throughout the grains as a result of HPT processing and that rearrange and aggregate to form dislocation cells in order to reduce the total strain energy. Subsequently, dislocation rearrangement develops increasing the misorientation between the cells (crystal rotation) thereby causing the formation of low-angle and then high-angle grain boundaries. Hence, elongated grains are subdivided, and equiaxed grains form through HPT processing. The newly formed nanograins show dislocation tangles and moire patterns inside them, which are evidences for high density of dislocations.[36] The elongated grains and low-angle grain boundaries caused by dislocation arrangement predominantly distribute in CCM_{HPT} at $\varepsilon_{eq} = 2.25$, which may result in promising mechanical properties according to a previous study.[9] For CCM_{HPT} processed at $\varepsilon_{eq} = 4.5$, the elongated-grains microstructure is not as predominant as in CCM_{HPT} processed at $\varepsilon_{eq} = 2.25$. This is because increasing ε_{eq} results in further refinement of elongated grains, thereby inducing a decrease in their prevalence, length, and width. The schematic illustration for the two grain refinement mechanisms as mentionaboved was given in Fig. 5.

The existence of two different grain refinement mechanisms raises the question that what affects the preference towards to either of the grain refinement mechanisms. Previ-

ously, it was suggested by Kireeva and Chumlyakov that <110>-oriented austenitic grains (fcc) transformed to martensites most easily during the tension in single-crystal Fe-Cr-Ni stainless steels,[42] and it was observed that <100>-oriented austenitic grains that were parallel to the rolling direction showed slower transformation, whereas the <111>-oriented grains that were parallel to the rolling direction showed much faster transformation in rolled stainless steel.[43] In addition, based on calculated Schmid factors, Zang *et al.* reported the easy martensitic transformation in Cube- and Goss-oriented austenitic steel during tension and the difficulty in martensitic transformation in <111>-oriented austenite during compression.[44] Based on these results, it can be inferred that the preference towards to either of grain refinement mechanisms might be related to the initial orientations of the γ-phase grains in the CCM alloy. If the initial grain orientations are suitable for martensitic transformation, grain refinement is more likely to occur over the mechanism that closely related to the $\gamma \rightarrow \varepsilon$ martensitic transformation.

The dislocation density of the CCM alloy significantly increased through HPT processing, as per Fig. 6. The dislocation density of CCM_{HPT} alloys reached the maximum value at $\varepsilon_{eq} = 9$, which indicated that an equilibrium state between generation and annihilation of dislocations was achieved in this condition. Maximum values of dislocation density in γ and ε phases of CCM_{HPT} processed at $\varepsilon_{eq} = 9$ are $2.8 \times 10^{16}\ m^{-2}$ and $3.8 \times 10^{16}\ m^{-2}$, respectively which are higher than those of other metals, i.e., Cu,[45] Al[12] and Al-Mg[46] alloys subjected to SPD, and similar to that of Ti-29Nb-13Ta-4.6Zr (TNTZ) subjected to HPT.[9] Dislocation density of CCM_{HPT} decreases at $\varepsilon_{eq} > 9$. This is because that the annihilation of dislocations becomes more predominant than the generation of dislocations thereby causing a decrease in dislocation density. In a previous study about CCM_{HPT},[25] it was reported that low-angle grain boundaries in CCM_{HPT} processed at $\varepsilon_{eq} \leq 9$ could transform to high-angle grain boundaries in CCM_{HPT} when ε_{eq} increases to 45. This result shows a correspondence to the occurrence of annihilation of dislocations and decreasing of dislocation density in CCM_{HPT} with a further increased ε_{eq}.

Figure 7 showed the subgrain diameters of γ phase and ε phase in CCM_{HPT} at various ε_{eq} compared to those of CCM_{CR}. The subgrain diameter of γ phase in CCM_{HPT} was lower than that of CCM_{CR} and its value decreased to a minimum when ε_{eq} increases to 9, and then saturated with further increasing ε_{eq}. Previously, it has been reported that grain refinement by SPD is controlled by a dynamic balance between hardening rate due to dislocation accumulation and recovery rate by dislocation annihilation, which finally results in an equilibrium structure with a minimum grain diameter and saturated dislocation density.[47] The minimum average grain diameter is determined by both intrinsic material properties and extrinsic processing conditions.[48–50] Therefore, the evolution of subgrain diameter of γ phase in CCM_{HPT} is closely related to the generation and annihilation behavior of dislocations caused by HPT-induced high strain. However, the subgrain diameter of ε phase in CCM_{HPT} is larger than that of CCM_{CR}; the value increases from $\varepsilon_{eq} = 2.25$ to $\varepsilon_{eq} = 9$, and then saturates. This phenomenon can be explained by the growth of ε phase under strain. It has been reported that the nucleation and formation of ε phase occur with the motion of Shockley partial dislocations.[20,35] Then, formed thin ε layers accumulate and it results in ε phase growth. Thus, the higher strain induced by HPT processing results in the formation of a large number of ε layers by dislocation gliding and accumulation; this leads to the formation of ε phases with larger subgrain diameter than that of CCM_{CR}. Then the subgrain diameter of ε phases in CCM_{HPT} increases with increasing strain which promotes the formation and accumulation of ε layers, and it finally saturates which is considered to be related to the balance between generation and annihilation of dislocations at subgrain boundaries.

XRD profiles provide information about the screening of strain fields, which is related to dislocation density and dislocation arrangement. If the strain fields of individual dislocations are screening each other, the total distortion in the lattice is lower that yields a smaller value of R_e. Strong screening of strain fields of dislocations occurs when dislocations are arranged into dipoles or low-angle grain boundaries. As the screening of strain fields of dislocations becomes stronger, the value of the dislocation arrangement parameter (M) becomes smaller, which suggests the better arrangement of dislocations. Figure 8 showed that except for the M parameter of the ε phase in CCM_{HPT} processed at $\varepsilon_{eq} = 2.25$, all other M parameters showed values smaller than 1, indicating that dislocations were suitably arranged in CCM_{HPT}. The M parameter values of the γ and ε phases in CCM_{HPT} decrease with increasing ε_{eq}, which indicates the development in the dislocation rearrangement with increasing strain.

4.2 Effects of microstructural evolution on mechanical properties

Figure 9 exhibited the tensile properties of CCM alloys. The UTS of CCM_{HPT} processed at $\varepsilon_{eq} = 2.25$ (~1709 MPa) was much greater than that of CCM_{ST} (~1041 MPa). This increase in the UTS is due to the increased volume fraction of the ε phase,[19,34] formation of nanostructured subgrains surrounded with low-angle grain boundaries, and accumulation of dislocations induced by HPT processing and grain refinement.[10,51,52] Tensile properties of CCM_{HPT} processed at $\varepsilon_{eq} = 2.25$, which has the highest tensile strength among all CCM_{HPT} conditions in our study, were compared with those of the other CCM alloys including fine-grained and bimodal structured CCM alloys. Hot forged CCM alloy (CCM_{HF}) reported by Yamanaka *et al.*[53], which shows the smallest average grain diameter compared to other CCM alloys in literature, was selected as fine-grained CCM alloy for comparison. The UTS and 0.2% proof stress of CCM_{HPT} processed at $\varepsilon_{eq} = 2.25$ (~1709 MPa and ~1528 MPa) are even greater than those of CCM_{HF} (~1450 MPa and ~1330 MPa). In addition, the UTS of CCM_{HPT} processed at $\varepsilon_{eq} = 2.25$ is also greater than that of bimodal structured CCM alloy (~1300 MPa)[53]. Abovementioned phenomenon is attributed to that the average grain diameter of CCM_{HPT} processed at $\varepsilon_{eq} = 2.25$ in nanometerscale (~84 nm) is smaller than that of CCM_{HF} (~0.8 μm)[53] and bimodal structured CCM alloy consisting of fine-grained and coarse-grained regions, which has an average grain diameter around 2–5 μm in fine-grained region and 36.8 μm in coarse-grained region[54]. The UTS of CCM_{HPT} was still high but decreases slightly at $\varepsilon_{eq} = 18$ in comparison

to those at $\varepsilon_{eq} = 2.25$ and 9, and it subsequently saturated at $\varepsilon_{eq} > 18$. Further, 0.2% proof stress of CCM_{HPT} was almost constant with increasing ε_{eq} from 2.25 to 18, and then it decreased at $\varepsilon_{eq} = 45$. This slight decrease in the strength is attributed to a slight decrease in the volume fraction of the ε phase and decrease in the dislocation density. The decrease in the M parameters with increasing ε_{eq} also shows a good correspondence to the arrangement of dislocations in subgrain boundaries, and evolution of low-angle grain boundaries to high-angle grain boundaries. Considering the abovementioned results of CCM_{HPT} processed at $\varepsilon_{eq} = 2.25$, it is concluded that HPT processing causes a drastic increase in tensile strength. However, HPT processing results in a significant lost in ductility and CCM_{HPT} becomes almost brittle. The elongation of CCM_{HPT} processed at $\varepsilon_{eq} = 2.25$ (~1%) is comparable with that of CCM_{HF} (~2.5%), even if the volume fraction of ε phase in CCM_{HPT} processed at $\varepsilon_{eq} = 2.25$ (~87%) is much higher than that in CCM_{HF} (~13%)[53].

By considering the hardness variation from the disk center, it is concluded that CCM_{HPT} processed at $\varepsilon_{eq} = 9$ ($N = 1$) shows the highest hardness at different positions from the center to the edge owing to the highest dislocation density and highest strain, according to previous results on the HPT processed CCM alloys.[25] Hardness of CCM_{HPT} was compared with that of bimodal structured CCM alloy. Vickers hardness of CCM_{HPT} processed at $\varepsilon_{eq} = 9$ ($N = 1$) at half radius (~521 *HV*) is greater than those of fine-grained (~480 *HV*) and coarse-grained (~440 *HV*) regions of bimodal structured CCM alloy. The greater hardness obtained in CCM_{HPT} processed at $\varepsilon_{eq} = 9$ ($N = 1$) is attributed to its smaller grain diameter and higher volume fraction of the ε phase (the volume fraction of the ε phase is around 20% for bimodal structured CCM alloy)[54]. In addition, the hardness of CCM_{HPT} processed at $\varepsilon_{eq} = 9$ ($N = 1$) almost does not differ with increasing distance from the center of the specimen, r (2, 3, and 5 mm), which may be because of the achieved microstructural homogeneity.[9] This phenomenon is similar to that of austenitic steel,[55] pure Ni[56] and pure Cu.[57] The hardness at the edge position is greater than that at the center of the disk for the same N at CCM_{HPT} processed at $\varepsilon_{eq} = 2.25$, 18 and 45 ($N = 0.25$, 2 and 5), which is attributed to the increased ε_{eq} at the edge position according to (eq. (1)). The increase in the hardness is attributed to increase in the volume fraction of the ε phase and grain refinement.[25]

5. Conclusions

The grain refinement mechanisms, the evolution of the dislocation density, and relationship between microstructural evolution and mechanical properties in the CCM alloy subjected to HPT processing were investigated. The obtained results are as follows:

(1) $\gamma \rightarrow \varepsilon$ phase transformation occurs in CCM_{HPT} and the volume fraction of the ε phase drastically increases through HPT processing in comparison to that of CCM_{ST}.

(2) Two different grain refinement mechanisms are proposed for the CCM alloy through HPT processing: first, the formed ε martensitic platelets subdivide the γ grains thereby resulting in grain refinement. Second, elongated grains are subdivided into the equiaxed ultrafine grains through formation and development of subgrains and $\gamma \rightarrow \varepsilon$ phase transformation.

(3) The dislocation densities in the γ and ε phases in HPT processed CCM alloys increase with increasing ε_{eq} and reach their maximum values of $\sim 2.8 \times 10^{16}\ m^{-2}$ and $\sim 3.8 \times 10^{16}\ m^{-2}$, respectively, at $\varepsilon_{eq} = 9$, which suggests the achievement of a balance between generation and annihilation of dislocations. The dislocation densities of the γ and ε phases tend to decrease and their subgrain diameters tend to saturate with further increasing ε_{eq} to the value over 9.

(4) The UTS of the CCM alloy significantly increases with HPT processing to $\varepsilon_{eq} = 2.25$. Further, it slightly decreases in CCM_{HPT} processed at $\varepsilon_{eq} = 18$ attributed to the decreased volume fraction of the ε phase and reduced dislocation density, and then, it saturates.

(5) The hardness of CCM_{HPT} increases with increasing distance from the center of the disk. Additionally, the hardness saturates with increasing ε_{eq} at the half-radius position and the edge position of the specimen. This saturation in hardness is attributed to the achievement of microstructural homogeneity along the radial direction of the specimen with increasing ε_{eq}.

Acknowledgement

This study was supported in part by a Grant-in-Aid for Scientific Research (A) No. 24246111 from the Japan Society for the Promotion of Science (JSPS) and the Inter-University Cooperative Research Program "Innovation Research for Biosis-Abiosis Intelligent Interface" from the Ministry of Education, Culture, Sports, Science and Technology (MEXT), Japan. This work was also supported in part by "The Yildiz Technical University Scientific Research Fund" under contract No. 2016-07-02-KAP01. The HPT process was carried out in the International Research Center on Giant Straining for Advanced Materials (IRC-GSAM) at Kyushu University.

REFERENCES

1) P.W. Bridgman: Phys. Rev. **48** (1935) 825–847.
2) A.P. Zhilyaev and T.G. Langdon: Prog. Mater. Sci. **53** (2008) 893–979.
3) R. Z. Valiev, R. K. Islamgaliev, and I.V. Alexandrov: *Bulk Nanostructured Materials from Severe Plastic Deformation*, 2000.
4) R.Z. Valiev, E.V. Kozlov, Y.F. Ivanov, J. Lian, A.A. Nazarov and B. Baudelet: Acta Metall. Mater. **42** (1994) 2467–75.
5) S. Scheriau, Z. Zhang, S. Kleber and R. Pippan: Mater. Sci. Eng. A **528** (2011) 2776–86.
6) Y. Iwahashi, Z. Horita, M. Nemoto and T.G. Langdon: Acta Mater. **45** (1997) 4733–41.
7) Y. Mine, S. Matsumoto, and Zenji Horita: Corros. Sci., 2011, vol. **53**, pp. 2969–77.
8) M. Kawasaki, B. Ahn and T.G. Langdon: Acta Mater. **58** (2010) 919–30.
9) H. Yilmazer, M. Niinomi, K. Cho, M. Nakai, J. Hieda, S. Sato and Y. Todaka: Acta Mater. **80** (2014) 172–82.
10) H. Yilmazer, M. Niinomi, M. Nakai, K. Cho, J. Hieda, Y. Todaka and T. Miyazaki: Mater. Sci. Eng. C **33** (2013) 2499–2507.
11) C. Xu, Z. Horita and T.G. Langdon: Acta Mater. **56** (2008) 5168–76.
12) Y. Ito and Z. Horita: Mater. Sci. Eng. A **503** (2009) 32–36.
13) R.B. Figueiredo and T.G. Langdon: Mater. Sci. Eng. A **528** (2011) 4500–4506.
14) A.A. Karimpoor, U. Erb, K.T. Aust and G. Palumbo: Scr. Mater. **49** (2003) 651–56.

15) K. Edalati, S. Toh, M. Arita, M. Watanabe and Z. Horita: Appl. Phys. Lett. **102** (2013) 181902.
16) Y. Koizumi, S. Suzuki, K. Yamanaka, B.S. Lee, K. Sato, Y. Li, S. Kurosu, H. Matsumoto and A. Chiba: Acta Mater. **61** (2013) 1648–61.
17) B. D. Ratner, A. S. Hoffman, F. J. Schoen, and J. E. Lemons: *Biomaterials Science - An Introduction to Materials in Medicine*, 1996.
18) S.H. Sun, Y. Koizumi, S. Kurosu, Y. Ping Li, H. Matsumoto and A. Chiba: Acta Mater. **64** (2014) 154–68.
19) T. Mitsunobu, Y. Koizumi, B.S. Lee, K. Yamanaka, H. Matsumoto, Y. Li and A. Chiba: Acta Mater. **81** (2014) 377–85.
20) K. Yamanaka, M. Mori, Y. Koizumi and A. Chiba: J. Mech. Behav. Biomed. Mater. **32** (2014) 52–61.
21) K. Yamanaka, M. Mori and A. Chiba: Acta Biomater. **9** (2013) 6259–67.
22) R.Z. Valiev and T.G. Langdon: Prog. Mater. Sci. **51** (2006) 881–981.
23) D.H. Shin, I. Kim, J. Kim and K.Tae. Park: Acta Mater. **49** (2001) 1285–92.
24) X. Wu, N. Tao, Y. Hong, G. Liu, B. Xu, J. Lu and K. Lu: Acta Mater. **53** (2005) 681–91.
25) M. Isik, M. Niinomi, K. Cho, H. Liu, M. Nakai, H. Yilmazer, Z. Horita and T. Narushima: J. Mech. Behav. Biomed. Mater. **59** (2016) 226–35.
26) J. Kratochvíl, M. Kružík and R. Sedláček: Acta Mater. **57** (2009) 739–48.
27) C.W. Su, L. Lu and M.O. Lai: Mater. Sci. Eng. A **434** (2006) 227–36.
28) G. Zhao, S. Xu, Y. Luan, Y. Guan, N. Lun and X. Ren: Mater. Sci. Eng. A **437** (2006) 281–92.
29) L. Li, T. Ungár, Y.D. Wang, G.J. Fan, Y.L. Yang, N. Jia, Y. Ren, G. Tichy, J. Lendvai, H. Choo and P.K. Liaw: Scr. Mater. **60** (2009) 317–20.
30) J. Gubicza, G. Ribárik, A. Borbély and T. Ungár: J. Appl. Crystallogr. **34** (2001) 298–310.
31) T. Ungár and G. Tichy: Phys. Status Solidi **171** (1999) 425–34.
32) G. Ribárik: J. Appl. Crystallogr. **34** (2001) 669–76.
33) T. Ungár, I. Dragomir, Á. Révész, and a. Borbély: J. Appl. Crystallogr. **32** (1999) 992–1002.
34) A. Chiba, K. Kumagai, N. Nomura and S. Miyakawa: Acta Mater. **55** (2007) 1309–18.
35) M. Mori, K. Yamanaka, H. Matsumoto and A. Chiba: Mater. Sci. Eng. A **528** (2010) 614–21.
36) X.M. Feng and T.T. Ai: Trans. Nonferrous Met. Soc. China **19** (2009) 293–98.
37) J. Gubicza: *X-Ray Line Profile Analysis in Materials Science*, IGI Global, 2014.
38) J.Z. Lu, K.Y. Luo, Y.K. Zhang, G.F. Sun, Y.Y. Gu, J.Z. Zhou, X.D. Ren, X.C. Zhang, L.F. Zhang, K.M. Chen, C.Y. Cui, Y.F. Jiang, X. Feng and L. Zhang: Acta Mater. **58** (2010) 5354–62.
39) M. Kawasaki and T.G. Langdon: Mater. Sci. Eng. A **498** (2008) 341–48.
40) G.P. Zheng, Y.M. Wang and M. Li: Acta Mater. **53** (2005) 3893–3901.
41) N. Hansen: Scr. Mater. **51** (2004) 751–53.
42) I.V. Kireeva and Y.I. Chumlyakov: Mater. Sci. Eng. A **481–482** (2008) 737–41.
43) E. Nagy, V. Mertinger, F. Tranta, and J. Sólyom: 2004, vol. 378, pp. 308–13.
44) M. Zhang, P. M. Kelly, and J. D. Gates: 1999, vol. 275, pp. 251–56.
45) J. Gubicza, N.H. Nam, L. Balogh, R.J. Hellmig, V.V. Stolyarov, Y. Estrin and T. Ungár: J. Alloy. Compd. **378** (2004) 248–52.
46) J. Gubicza, N.Q. Chinh, Z. Horita and T.G. Langdon: Mater. Sci. Eng. A **387–389** (2004) 55–59.
47) H. Wen, R.K. Islamgaliev, K.M. Nesterov, R.Z. Valiev and E.J. Lavernia: Philos. Mag. Lett. **93** (2013) 481–89.
48) F.A. Mohamed: Acta Mater. **51** (2003) 4107–19.
49) F.A. Mohamed and S.S. Dheda: Mater. Sci. Eng. A **580** (2013) 227–30.
50) A.P. Zhilyaev, G.V. Nurislamova, B.K. Kim, M.D. Baró, J.A. Szpunar and T.G. Langdon: Acta Mater. **51** (2003) 753–65.
51) H. Yilmazer, M. Niinomi, M. Nakai, J. Hieda, Y. Todaka, T. Akahori and T. Miyazaki: J. Mech. Behav. Biomed. Mater. **10** (2012) 235–45.
52) S. Gourdet and F. Montheillet: Acta Mater. **51** (2003) 2685–99.
53) K. Yamanaka, M. Mori and A. Chiba: Metall. Mater. Trans., A Phys. Metall. Mater. Sci. **43** (2012) 5243–5257.
54) S.K. Vajpai, C. Savangrat, O. Yamaguchi, O.P. Ciuca and K. Ameyama: Mater. Sci. Eng. A **58** (2016) 1008–1015.
55) R. Valiev: Nat. Mater. **3** (2004) 511–16.
56) A.P. Zhilyaev, K. Oh-ishi, T.G. Langdon and T.R. McNelley: Mater. Sci. Eng. A **410–411** (2005) 277–80.
57) G. Sakai, K. Nakamura, Z. Horita and T.G. Langdon: Mater. Sci. Eng. A **406** (2005) 268–73.